Volume 4
Number 4
21 February 2023
Pages 979–1204

# Materials Advances

rsc.li/materials-advances

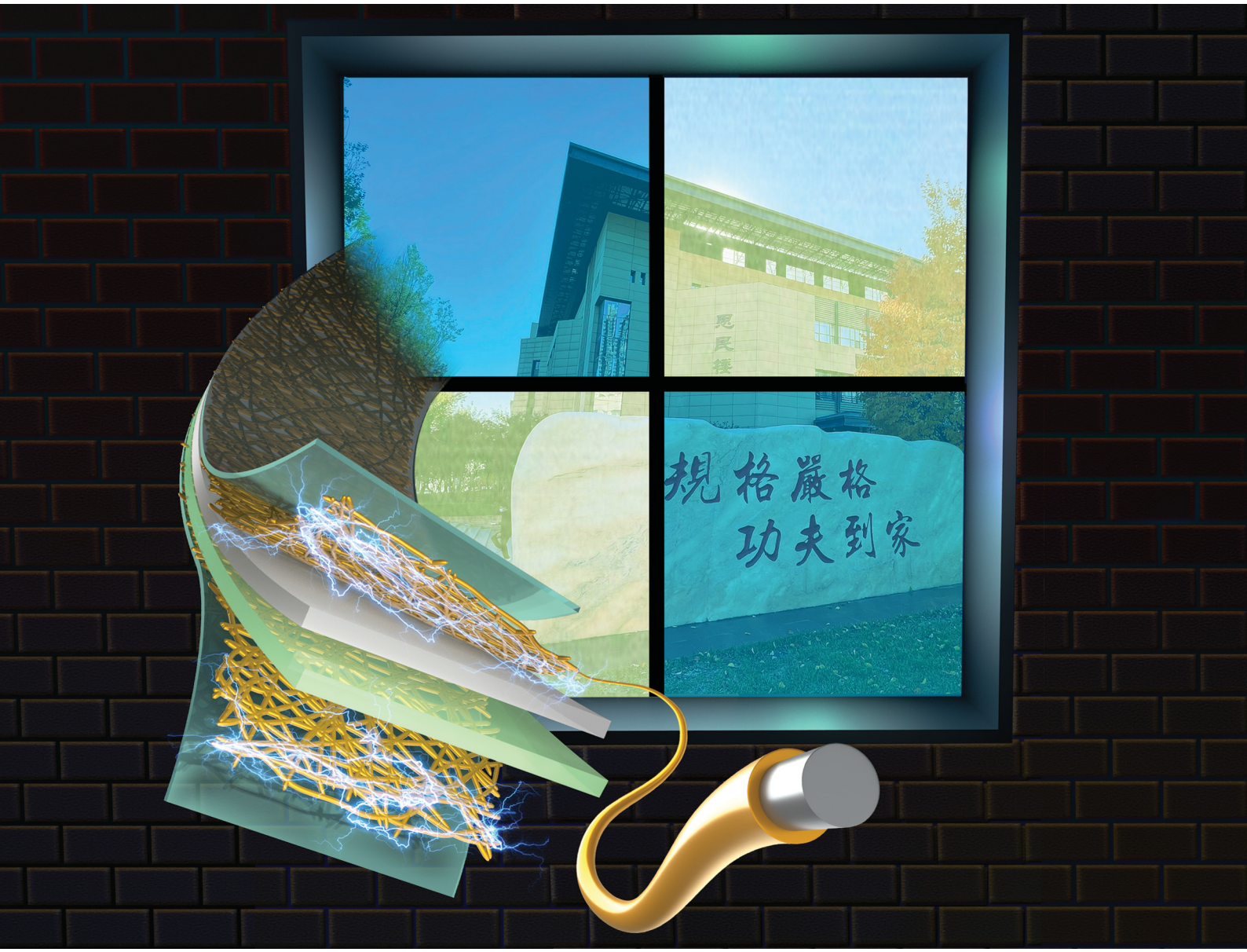


ISSN 2633-5409

ROYAL SOCIETY OF CHEMISTRY

**PAPER**

Fengyu Su, Yanqing Tian, Yanhong Tian *et al.*
An electrochemically stable Ag@Au–Co core–shell nanowire network-based transparent conductor for flexible self-powered Zn-based electrochromic smart devices

Materials Advances

ROYAL SOCIETY OF CHEMISTRY

PAPER

View Article Online
View Journal | View Issue



Cite this: *Mater. Adv.*, 2023, 4, 995

# An electrochemically stable Ag@Au–Co core–shell nanowire network-based transparent conductor for flexible self-powered Zn-based electrochromic smart devices†

He Zhang,[ab] Jiayun Feng,[a] Fangyuan Sun,[b] Dongyan Zhou,[b] Ge Cao,[b] Zhuohuan Wu,[a] Shang Wang,[a] Fengyu Su,*[c] Yanqing Tian*[bd] and Yanhong Tian*[a]

Silver nanowires (AgNWs) are important materials used to fabricate flexible transparent conductors (FTCs) for next-generation wearable electronics. However, the electrochemical instability still limits their practical application in electrochemical devices. Herein, highly stable FTCs are demonstrated *via* coating an Au–Co alloy shell around an AgNW core by electrodeposition. The AgNW@Au–Co core–shell network exhibited excellent resistance against chemical (in $H_2O_2$ solution for 200 s) and electrochemical corrosion (electrochemical anodic corrosion in 1 M $H_2SO_4$ solution for 100 s). Meanwhile, the modified FTC also possessed good optoelectrical performance and high mechanical stability (2000 bending cycles) owing to the firm metallic bonding between the stacked NWs during the electrodeposition process. To evaluate the improvement in electrochemical stability, a prototype of a self-powered polyaniline electrochromic smart system based on the versatile AgNW@Au–Co network FTC was fabricated, and it exhibited a high optical modulation range (41.22%) and good energy-storage performance (4 mF $cm^{-2}$). Our strategy of introducing a protective alloy shell onto AgNW by electrodeposition opens a new door for realizing high-performance FTCs by a facile method to broaden their application in flexible electrochemical devices.

Received 15th November 2022,
Accepted 17th December 2022

DOI: 10.1039/d2ma01036d

rsc.li/materials-advances



## 1. Introduction

Transparent conductors (TCs) serve a critical function in a variety of applications in optoelectronics, including light-emitting diodes (LEDs),[1] solar cells,[2] flexible displays,[3,4] and electrochromic devices.[5–9] Indium tin oxide (ITO), which has high optical transmittance and low sheet resistance, is the most commonly used commercial transparent conductive material to fabricate TCs for these applications.[10–12] However, being a kind of ceramic material, the intrinsic brittleness of ITO is still a deterrent.[13–15] The recent interest in the revolution of optoelectronic devices from rigid to flexible has created an urgent need to seek an alternative material.[16–19] Compared with ITO-based TCs, silver nanowire (AgNW) networks possess significant advantages, such as excellent electrical conductivity, mechanical flexibility, transmittance, solution compatibility, and scalability.[20–23] The applications of AgNW networks have been expanding to various flexible devices. For instance, Chang *et al.* fabricated a bendable polymer fuel cell based on an AgNW FTC.[24–26] Moon *et al.* obtained an Ag/Au/Polypyrrole(PPy) core–shell NW network for flexible supercapacitors.[27] Lee fabricated a highly stretchable transparent supercapacitor using an Ag–Au core–shell NW network.[28] Hu *et al.* successfully fabricated a transparent capacitive sensor using an AgNWs/polyurethane conductive film.[29] A stretchable and transparent Kirigami conductor was successfully obtained by Won *et al.* for use in e-skin.[30] Park *et al.* realized the fabrication of an AgNW-coated fibrous air filter medium.[31] Jeong obtained an active $PM_{2.5}$ filter based on an AgNW network.[32] Ko *et al.* fabricated color-changing soft robots with AgNWs.[33–36]

However, the electrochemical instability problem of AgNW networks is still the major obstacle that prevents their application in electrochemical devices, such as supercapacitors, and

[a] *State Key Laboratory of Advanced Welding and Joining, Harbin Institute of Technology, Harbin 150001, China. E-mail: tianyh@hit.edu.cn*
[b] *Department of Materials Science and Engineering, Southern University of Science and Technology, Shenzhen 518055, China*
[c] *Academy for Advanced Interdisciplinary Studies, Southern University of Science and Technology, Shenzhen 518055, China. E-mail: fysu@sustech.edu.cn*
[d] *Key Laboratory of Energy Conversion and Storage Technology (Southern University of Science and Technology), Ministry of Education, Shenzhen 518055, China. E-mail: tianyq@sustech.edu.cn*

† Electronic supplementary information (ESI) available. See DOI: https://doi.org/10.1039/d2ma01036d

electrochromic devices (ECDs).[37–39] The critical failure mode is when AgNWs easily dissolve in the electrolyte, resulting in disconnection and loss of conductivity. Previous works have made many attempts to prevent this phenomenon by encapsulating the AgNW network with protective materials, including PEDOT:PSS,[40] graphene,[41] and metal oxides.[33] For example, Shinde *et al.* wrapped the AgNWs with benzotriazole and a $TiO_2$:Cs layer to fabricate a flexible $WO_3$-ECD, which remained stable after 100 electrochemical redox cycles.[42] Aghazadehchors *et al.* fabricated a $ZnO/Al_2O_3$-coated AgNW network, which exhibited improved thermal stability with minimal transparency loss.[43] A thermal and electrically stable AgNW network was realized by depositing ZnO coatings.[44] Chang *et al.* fabricated a thermally stable Ag@$ZrO_2$ core–shell nanowire network by atomic layer deposition. A flexible supercapacitor was successfully achieved using the AgNWs/PEDOT:PSS hybrid electrode because the PEDOT:PSS layer provided significantly improved resistance against the electrochemical corrosion of the AgNW network.[45] However, the poor intrinsic conductivity of these materials usually has a negative effect on their optoelectrical performance. Moreover, these materials are usually spin-coated onto the whole electrode without selectivity, which would block the blank area in the network and reduce the transmittance.[46]

Besides coating a protective layer onto the AgNW network, Other structures have been explored to improve the AgNW stability. For example, Kumar *et al.*[47] fabricated a graphene/AgNWs/graphene conductor with good resistance to oxidation and mechanical flexibility. An aluminum-doped zinc oxide (AZO)/AgNWs/AZO FTC was obtained by Xu *et al.* with enhanced thermal stability.[48] Liu *et al.* successfully embedded octadecanethiol-decorated AgNWs into an epoxy resin, which exhibited excellent resistance against high temperatures and chemical corrosion of $Na_2S$.[49] In another work, a thermally stable ZnO–Ag NW-Polyimide FTC was fabricated, and a white polymer light-emitting diode was obtained.[50] However, these works have not paid enough attention to electrochemical stability.

To improve electrical conductivity, many methods have been developed to weld the NWs together. For example, Joule heating has proved to be an effective method to join AgNWs.[51] Tukuno *et al.* welded stacked NWs by mechanical pressing.[52] Celano *et al.* realized capillarity-driven welding of semiconductor NWs to form Ohmic junctions.[53] Lee *et al.* soldered AgNWs using a conductive polymer to improve electrical conductivity, and a flexible touch panel was obtained.[54] Laser nano-welding is also an effective method to weld the AgNWs network and enhance conductivity.[55–57] Lee *et al.* joined AgNWs *via* carbon nanotubes (CNTs) to achieve a stretchable transparent conductor, which exhibited excellent conductivity. Although these methods achieved firm welding of NWs and reduced contact resistance, they could not improve the electrical stability at the same time.

Electrochromic smart windows can present different color responses when different voltages are applied and are attracting increasing interest in reducing energy consumption.[58–62] In contrast to rigid ECDs, flexible ECDs can be installed onto pristine glass windows without replacing them.[63] Moreover, they can be adapted to non-planar-shaped windows because of their intrinsic conforming ability. Conductive polymers with low cost, excellent mechanical flexibility and processability are attracting increasing interest in electrochemical devices.[64–67] Recently, some important advances have been made in the fabrication of flexible electrochemical devices based on conductive polymers. For instance, Guo *et al.* successfully fabricated an electrochromic energy-storage device using polyaniline (PANI)-stabilized tungsten oxide, which exhibited a coloration efficiency of 98.4 $cm^2\ C^{-1}$ and an areal capacitance of 0.025 F $cm^{-2}$.[68] Zhou *et al.* fabricated a multicolour PANI electrochromic film with a reversible color-changing ability from yellow to purple.[63] Yuksel fabricated a supercapacitor based on coaxial AgNW/PPy nanocomposite with a long cycle life.[69] However, these flexible ECDs still need an external power supply, which would involve extra energy consumption.[70] Self-powered ECDs with metal Zn as the counter electrode have become a hot research area[71] as they can realize zero energy consumption and simplify the installation, while reports on self-powered flexible PANI ECDs are still pretty scarce.

Constructing core–shell structures has been considered an effective method to fabricate highly stable NW-based FTCs.[72] For example, Stewart *et al.* synthesized Cu@Ag, Cu@Au and Cu@Pt core–shell NWs with anti-oxidation performance for use in FTCs.[73] Due to the excellent electrical conductivity and chemical stability, the Au–Co alloy is widely used in the electronic industry as the gold finger material on printed circuit boards,[74] which inspired us to use the Au–Co alloy as an inhibitor to prevent AgNWs from electrochemical corrosion. Therefore, in this work, a passive Au–Co alloy shell was conformally and selectively coated around the AgNW shell by using a facile and simple electrodeposition method, which could provide good protection and avoid the extensive decrease in transmittance. Moreover, the stacked AgNWs were welded together during the electrodeposition process. Thus, the sheet resistance was also significantly decreased due to the reduction in contact resistance between the stacked NWs. Based on these modifications, we successfully fabricated a self-powered flexible ECD prototype using polyaniline (PANI) as the electrochromic material and metal Zn as the counter electrode, which demonstrated great potential for application in energy-efficient flexible electronics.

## 2. Experimental methods

### 2.1. Fabrication of the transparent AgNW@Au–Co network conductor

The AgNW ink with an average diameter of 20–25 nm and length of 20–40 μm (purchased from Zhejiang Kechuang Advanced Materials Technology Co., Ltd.) was washed 3 times with isopropanol and deionized water in sequence. Polyvinyl pyrrolidone ($M_w$ = 800 000) was used in the synthesis process of AgNWs. After washing, the obtained AgNW ink was adjusted to a concentration of 0.05 mg $mL^{-1}$. For fabricating the flexible TC (FTC), the AgNWs were coated onto a flexible polyethylene

terephthalate (PET) polymer substrate with a thickness of 100 μm and transmittance of 90.6% (at 550 nm, Fig. S1, ESI†) using the vacuum filtration method to form a conductive network. The AgNW ink was first filtered using a 45 μm microporous filtration membrane to form the network. Then, the AgNW network was transferred onto the flexible PET substrate by mechanical pressing. The vacuum filtration installation is shown in Fig. S2 (ESI†). The PET substrate was washed using acetone and absolute ethyl alcohol. Then, the Au–Co shell was electrodeposited around the AgNW core using a two-electrode electrodeposition system. The AgNW FTC was connected as the cathode, and the graphite sheet was connected as the anode. The electrolyte was prepared according to previous reports;[75] it contained $CoSO_4{\cdot}7H_2O$ (16.8 g $L^{-1}$), citric acid (140 g $L^{-1}$), KOH (120 g $L^{-1}$), and $KAu(CN)_2$ (3.2 g $L^{-1}$). The electrodeposition process was performed under a constant current density (1 mA $cm^{-2}$) for 10 s.

### 2.2. Fabrication of the self-powered electrochromic device

The PANI layer was deposited onto the AgNW@Au–Co FTC using the electropolymerization method in an electrochemical workstation (CHI660E, CHENGHUA, China) with a three-electrode system. The AgNW@Au–Co FTC was connected as the green working electrode, a Pt sheet was connected as the red counter electrode, and Ag/AgCl was connected as the white reference electrode. The electropolymerization process was carried out under a current density of 0.1 mA $cm^{-2}$ for 700 s. The electrolyte used for depositing PANI contained 0.5 mol $L^{-1}$ $H_2SO_4$ and 0.25 mol $L^{-1}$ aniline in absolute ethyl alcohol. After the PANI electrode was obtained, double sticky tape with a thickness of 125 μm was fixed around the PANI electrode as a supporting frame. Then, the metal Zn strip was placed on the double sticky tape. Subsequently, 1 mol $L^{-1}$ $ZnCl_2$ solution was dropped into the frame. Then, another piece of PET without AgNWs was placed on top. At last, the device was sealed using UV curing adhesive.

### 2.4. Characterization

We observed the morphologies of the AgNW and AgNW@Au–Co networks by scanning electron microscopy (SEM, MIR-A3XMH, TESCAN, Czech). The crystal structure was characterized by transmission electron microscopy (TEM, Tecnai G2 F30, FEI, America). The surface chemical state was characterized using an X-ray photoelectron spectrometer (XPS, PHI 5400, ULVAC-PHI, Japan) equipped with an Al Kα X-ray (1486.6 eV) source. The transmittance was measured using an ultraviolet spectrophotometer (Lambda 650S, PerkinElmer, America). The transmittance of FTC was measured relative to that of PET (The transmittance of PET was set as 100%). The transmittance of ECD was measured relative to that of the air (The transmittance of air is set as 100%). The sheet resistance of FTC was measured using a surface resistivity meter (MCP-T370, Mitsubishi, Japan).

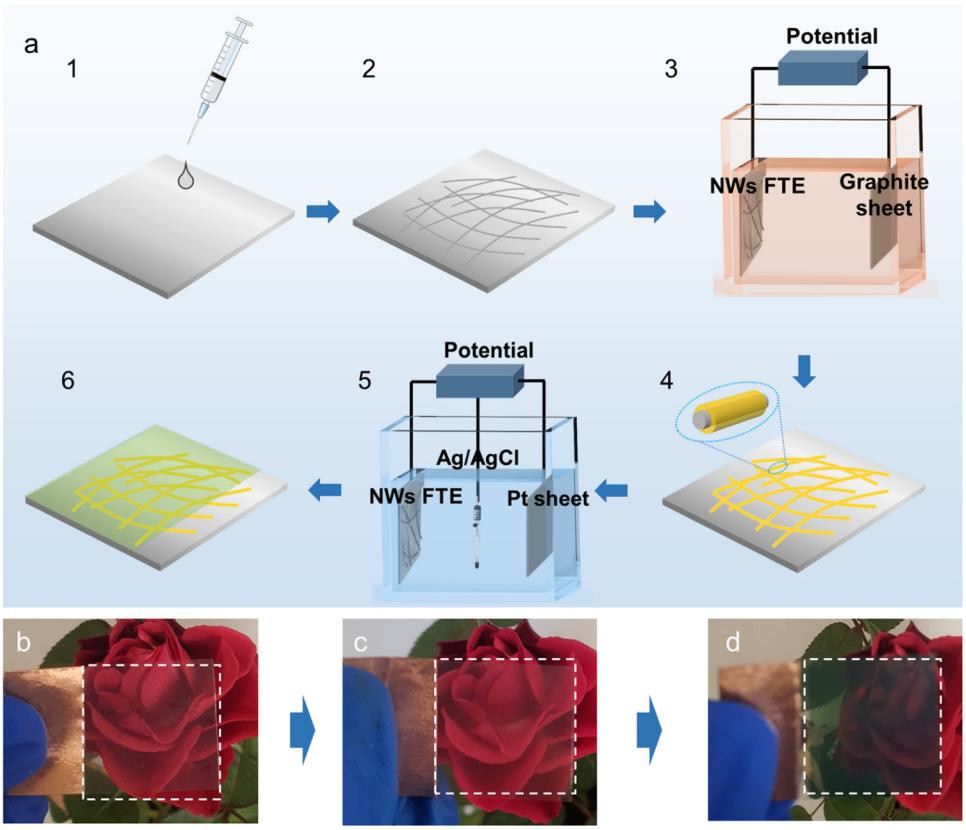


Fig. 1 (a) Schematic illustration of electrodeposition toward fabricating the AgNW@Au–Co network FTC and the PANI electrochromic film. The optical image of (b) the AgNW network FTC, (c) the AgNW@Au–Co network FTC and (d) the PANI electrochromic film.

The electrochemical test was performed in an electrochemical station (CHI660E, CHENGHUA, China). The cyclic voltammetry (CV) curves were collected to measure the electrochemical redox behaviours of different samples. Galvanostatic charge–discharge (GCD) tests were performed to obtain the areal capacitance. The areal capacitance was calculated using the following formula:[76]

$$C = (I^*\Delta t)/(\Delta U)$$

where $I$, $\Delta t$, and $\Delta U$ represent the areal current density, discharge time and voltage window, respectively.

## 3. Results and discussion

### 3.1. Fabrication of the Ag@Au–Co nanowire network

Fig. 1a schematically shows the experimental process. Firstly, the AgNW ink was uniformly distributed on the surface of a flexible PET polymer substrate to obtain the AgNW network. Then, the conductive AgNW network was set as the cathode. After the power was turned on, Au and Co ions in the electrolyte were reduced to atoms and deposited onto the AgNW network FTC under the driving force of the current. Because only the NW network was conductive, the Au–Co layer was selectively deposited around the AgNWs, and the core–shell structure could be formed. The passive Au–Co alloy layer could significantly improve the electrochemical stability of the pristine AgNW network. As a result, the PANI electrochromic layer was anodically electropolymerized onto the modified FTC. Fig. 1b–d exhibit the optical images of the AgNW network FTC, the AgNW@Au–Co FTC and the PANI electrochromic film, respectively. The rose flower under the AgNW network FTC was clearly visible, suggesting excellent light transmittance (Fig. 1b). No apparent change was observed after the Au–Co layer was coated, which proved that the selective coating of the Au–Co shell had a negligible effect on transmittance (Fig. 1c). Moreover, the film changed color to green, indicating that the PANI layer was successfully deposited, as shown in Fig. 1d.

We collected the SEM images of the AgNW network before and after electrodeposition, as shown in Fig. 2a and b. In the pristine AgNW network, the upper NWs loosely overlapped the bottom ones, suggesting only physical contact between each other. Hence, it would be difficult for the electrons to pass the junction, and the electrical resistance is higher. By contrast, after electrodeposition, the gaps between stacked AgNWs were filled with Au and Co atoms, and firm joints between them were obtained at the junction region, as depicted in Fig. 2b. The

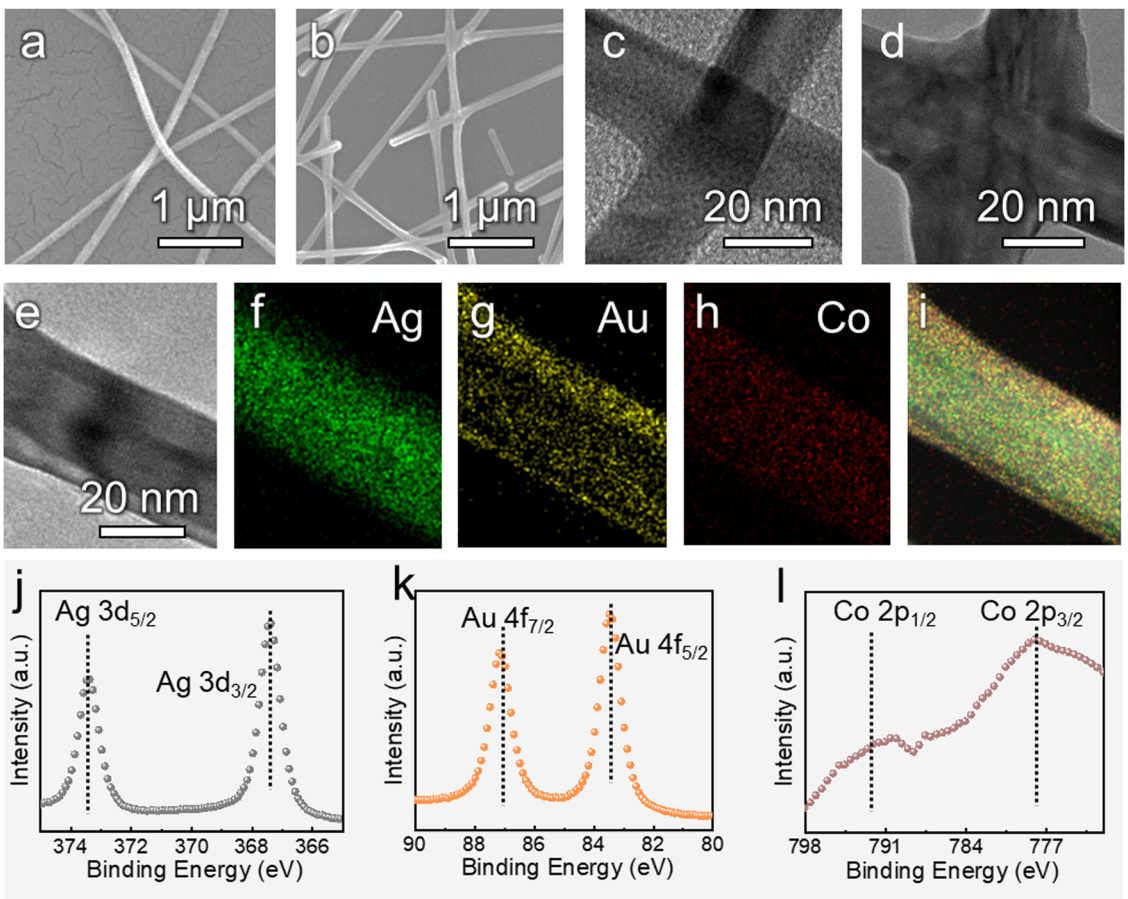


Fig. 2 The SEM images of the (a) AgNW network and (b) AgNW@Au–Co alloy network. The TEM images of (c) a loose junction before and (d) a tight junction after electrodeposition. (e–i) The TEM images and the corresponding Ag, Co and Au elemental distributions of the AgNW@Au–Co alloy. The XPS survey spectra:(j) Ag 3d; (k) Au 4f and (l) Co 2p.

Table 1 The elemental composition of Ag@Au–Co NWs

| Element | Weight % | Atomic % |
|---|---|---|
| Co(K) | 0.15 | 0.32 |
| Ag(L) | 65.23 | 77.22 |
| Au(L) | 34.62 | 22.45 |

upper NWs were obviously embedded into the bottom NWs, which would significantly facilitate the transfer of electrons. We further used TEM to characterize the morphologies of the AgNWs and Ag@Au–Co alloy NWs. As shown in Fig. 2c, before electrodeposition, the edges of the stacked NWs were clear and distinct. However, when the Au–Co alloy was deposited, the edges of the bottom and top NWs were merged together, suggesting firm metallurgical bonding (Fig. 2d). To prove the formation of the core–shell structure, EDS mapping was used to obtain the elemental distribution. Fig. 2e shows the morphology of an Ag@Au–Co alloy NW. The corresponding silver, gold, and cobalt elemental distributions are shown in Fig. 2f–i, respectively. The XPS spectra of silver, gold and cobalt are depicted in Fig. 2j–l, respectively. These characteristic peaks also confirm the formation of the alloy structure. We further measured the composition of the Au–Co alloy layer using EDS, as shown in Table. 1. The proportions of Co and Au elements were 1.41 at% and 98.59 at%, respectively. We further measured the thickness of the Au–Co alloy layer. As shown in Fig. S3 (ESI†), before the electrodeposition of the Au–Co alloy layer, the diameter of a pristine Ag NW was 20.12 nm. In contrast, the diameter increased to 31.25 nm later. Hence, the thickness of the Ag–Co layer was 5.57 nm.

### 3.2. Opto-electrical performance of the Ag@Au–Co nanowire network

Because of the metallic joints between stacked NWs, the electrical conductivity of the FTC was improved. Fig. 3a plots the changes in sheet resistance and transmittance with the electrodeposition time. Initially, the pristine AgNW network showed a sheet resistance of 180 Ohm per sq at a transmittance of 94.1%. After electrodeposition for 6 s, the sheet resistance decreased to 20 Ohm per sq at a transmittance of 85.2%, suggesting that the Au and Co atoms filling the gaps are beneficial for the transfer of electrons. With a further increase in electrodeposition time, sheet resistance exhibited a slight decrease, which indicated that the metallic bonding had formed in the first 6 s. We compared the optoelectrical performance of AgNW@Au–Co with AgNW and ITO FTC,[77] as shown in Fig. 3b. It was obvious that the FTC based on the AgNW@Au–Co network processed higher transmittance at similar sheet resistance, implying its excellent comprehensive optoelectrical performance. We further calculated the value of the figure of merit (FoM) at different electrodeposition times according to the following formula:[78]

$$\mathrm{FoM} = \frac{188.5\sqrt{T}}{R_s(1-\sqrt{T})}$$

where $R_s$ and $T$ are sheet resistance and transmittance,

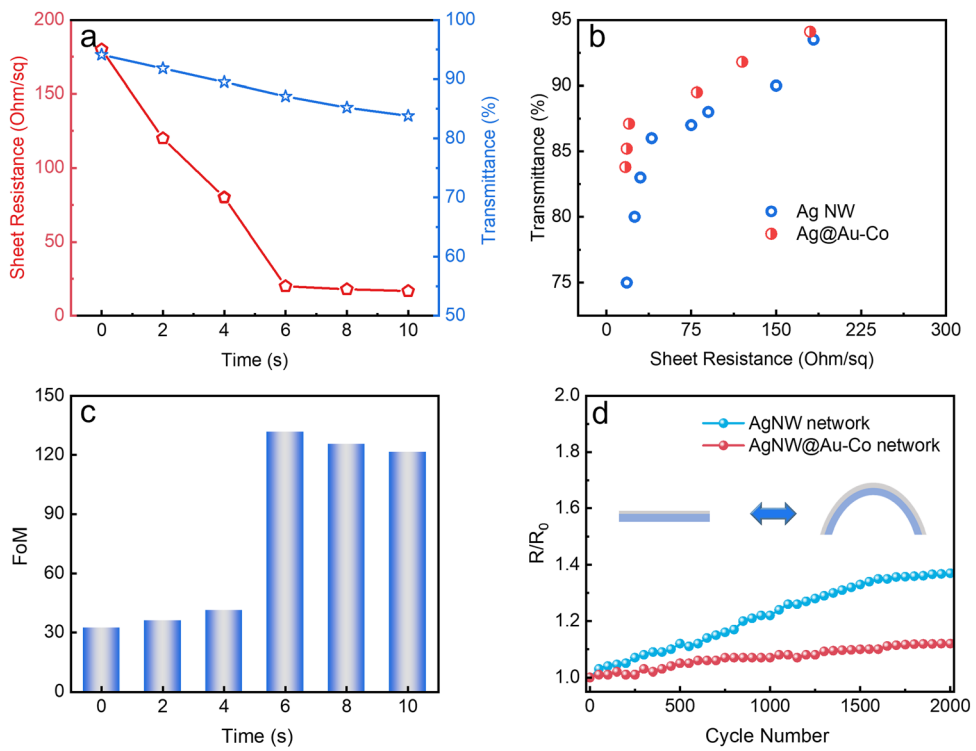


Fig. 3 (a) The sheet resistance and transmittance of the AgNW@Au–Co network FTC *vs.* electrodeposition time. (b) The transmittance of the AgNW and AgNW@Au–Co network FTCs as a function of sheet resistance. (c) The FoM of the AgNW@Au–Co network FTC *vs.* electrodeposition time. (d) Relative resistance variation of the AgNW FTC and the AgNW@Au–Co FTC during cyclic outward bending.

respectively. The FoM value of the original AgNW FTC was 32.39. Surprisingly, the FoM value reached 131.82 after electrodeposition for 6 s, proving the significant improvement in optoelectrical performance (Fig. 3c). Stability against mechanical deformation is of great importance for the actual usage of FTCs. We measured the mechanical stability of the AgNW and AgNW@Au–Co FTCs using the cyclic outward bending test with a radius of 6 mm, as shown in Fig. 3d. The resistance of the pristine AgNW FTC exhibited an obvious decline after 2000 bending cycles. In contrast, the modified AgNW@Au–Co FTC remained stable under the same condition. We also measured the change in relative resistance during cyclic inward bending. Similar to outward bending, the modified AgNW@Au–Co FTC again exhibited better stability, as shown in Fig. S4 (ESI†). This advance can be attributed to the firm joints between the stacked NWs, which strengthen the conductive network.

### 3.3. The stability of the Ag@Au–Co nanowire network

Stability against chemical corrosion is also an important index for FTCs. We measured the change in relative resistance after dropping them in a 15 wt% $H_2O_2$ solution, as schematically shown in the inset of Fig. 4a. The pristine AgNW network rapidly lost conductivity when dropped in the $H_2O_2$ solution. By contrast, the relative resistance of the modified AgNW@Au–Co network showed negligible change, indicating that the coated alloy layer significantly improved the chemical stability. The CV cures of the AgNW and AgNW@Au–Co networks are depicted in Fig. 4b. The pristine AgNW network showed a high oxidation peak, but no corresponding reduction peak was observed, suggesting that it had lost conductivity and failed. However, when the Au–Co alloy shell was coated around the AgNW core, a pair of redox peaks were observed, indicating its high resistance against electrochromic anodic corrosion. We further measured the electrochemical stability of the AgNW network and AgNW@Au–Co network when an anodic current density of 10 mA $cm^{-2}$ was applied. As depicted in Fig. 4c, the potential response of the pristine AgNW network rapidly increased beyond the measurement limit (10 V) within 10 s, while the AgNW@Au–Co alloy network remained stable after 100 s. These results also proved that the Au–Co alloy formed an effective layer against electrochemical corrosion. The morphologies of the AgNW and AgNW@Au–Co alloy networks after immersion in the $H_2O_2$ solution were characterized using SEM. The pristine AgNW network was seriously destroyed (Fig. 4d), and the FTC had lost conductivity. However, although some broken NWs could be observed in the AgNW@Au–Co alloy network, the NWs were still welded together and conductive, as shown in Fig. 4e. Similar to the results observed after chemical corrosion, many particles were observed in the AgNW network after

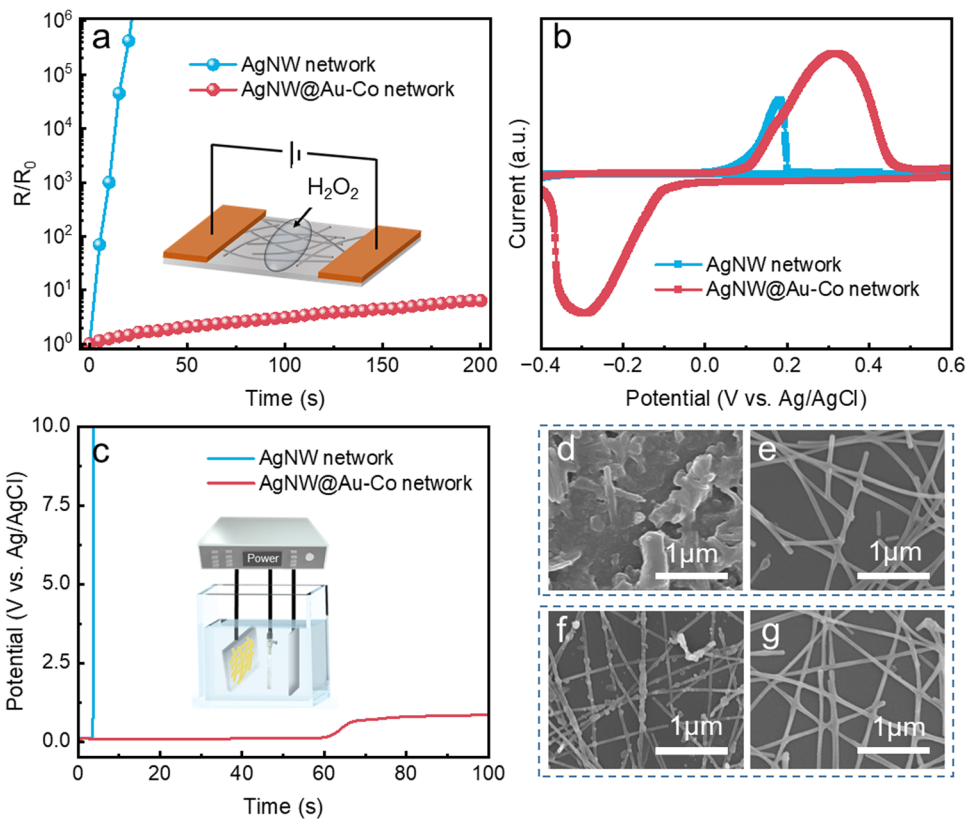


Fig. 4 (a) The relative resistance variation of the AgNW FTC and AgNW@Au–Co FTC after $H_2O_2$ corrosion. (b) The CV curves of the AgNW FTC and AgNW@Au–Co FTC. (c) The response potential (*vs.* Ag/AgCl) of the AgNW FTC and AgNW@Au–Co FTC against anode oxidation in 1 mol $L^{-1}$ $H_2SO_4$ solution. The SEM images of the (d) AgNW FTC and (e) AgNW@Au–Co FTC after $H_2O_2$ corrosion. The SEM images of the (f) AgNW FTC and (g) AgNW@Au–Co FTC after anode oxidation in 1 mol $L^{-1}$ $H_2SO_4$ solution.

electrochemical corrosion (Fig. 4f), while the AgNW@Au–Co network only showed slight changes (Fig. 4g). These results are also consistent with the aforementioned change in relative resistance.

### 3.4. Fabrication of the prototype of flexible self-powered ECD

Based on these improvements, we electropolymerized a PANI layer onto the FTC to fabricate an electrochromic device. During the electropolymerization process, the FTC was set as the anode. Hence, it was difficult to deposit the PANI layer onto the pristine AgNW FTE due to anodic electrochemical corrosion. As shown in Fig. 5a, the pristine AgNWs were severely destroyed. By contrast, a uniform PANI layer was electrodeposited onto the Ag@Au–Co NW FTE (Fig. 5b). Then, we assembled an ECD using metal Zn as the counter electrode, as shown in Fig. 5c. Surprisingly, this ECD also exhibited energy-storage properties. When we connected the two devices, the stored energy in the ECD successfully powered a red LED. Fig. 5d shows the CV curves of the ECD at different scanning rates. When the scanning rate was increased from 2 mV $s^{-1}$ to 10 mV $s^{-1}$, the shape of the CV curves showed negligible change, suggesting excellent rate performance. Fig. 5e exhibits the GCD curves of the ECD at different current densities. With increasing discharge current densities, the discharge time gradually decreased. Furthermore, we calculated the areal capacitance of the electrochromic device at different current densities. For example, when the discharge current density was 0.1 mA $cm^{-2}$, the areal capacitance was 4 mF $cm^{-2}$. We measured the CV curves (Scanning Rate: 100 mV $s^{-1}$) of the ECD in the flat and bent states (with a bent radius of 25 mm), as shown in Fig. S5 (ESI†). The CV curves showed a similar shape at the different states, suggesting the good flexibility of the ECDs.

Fig. 6a schematically exhibits the configuration of the ECD prototype based on the AgNW@Au–Co network FTC. In the daytime, when a solar cell was connected to the ECD, the potential caused by sunlight could drive the ECD to change to a deep blue color (Fig. 6b), which avoided excessive light intake indoors. In the night, when we want more light come to indoor, we short-circuited the two electrodes of the ECD. The ECD turned back to light green under the driving force of the internal potential (Fig. 6c). These results suggested the unique self-driving property of the ECD containing a metal as counter material. The conventional ECD can also be colored when driven by solar cells, but it cannot spontaneously bleach. In other words, the bleaching process needs an external energy supply. Fig. 6d shows the UV-visible absorption spectrum of the ECD in a wavelength range of 400–800 nm in the colored and bleached states. In the colored state, an obvious peak was observed at 633 nm, indicating low light transmittance. We measured the *in situ* change in transmittance in a sweeping voltage window from 0 V to 1.8 V, as depicted in Fig. 6e. When the input voltage was 1.8 V, the transmittance decreased to 26.15%.

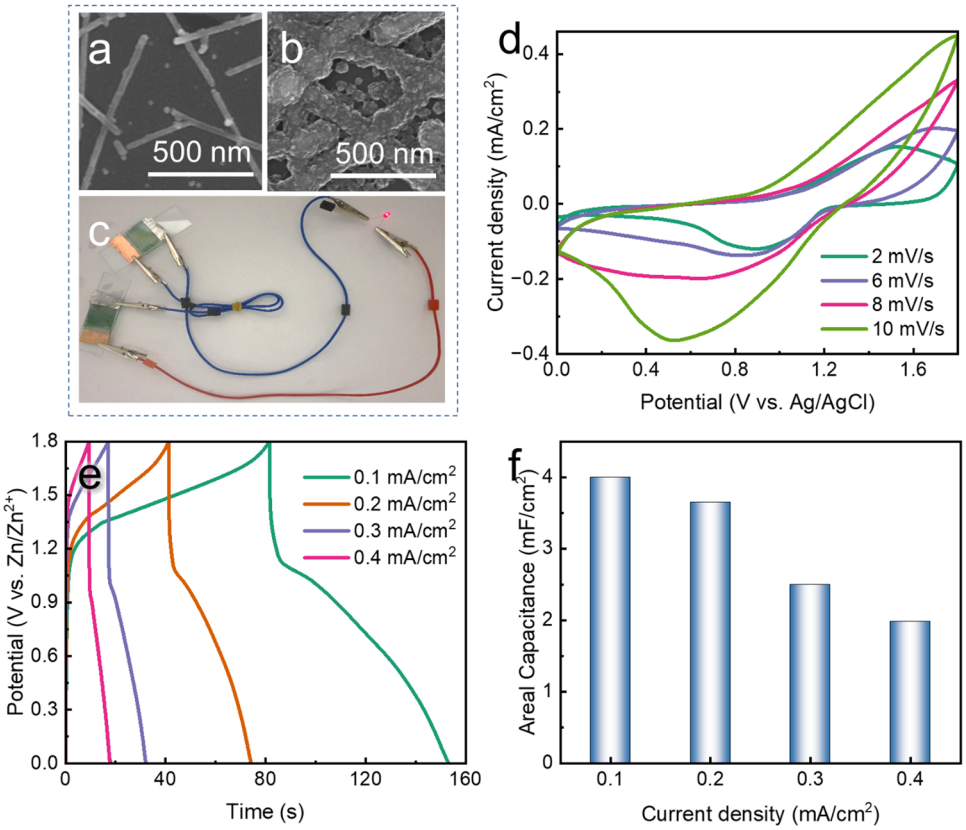


Fig. 5 The SEM images of the (a) AgNW FTC and (b) AgNW@Au–Co FTC after electropolymerization of PANI on the surface. (c) A red LED was powered by the ECD. (d) The CV and (e) GCD curves of the ECD. (f) The areal capacitances of the ECD at different discharge current densities.

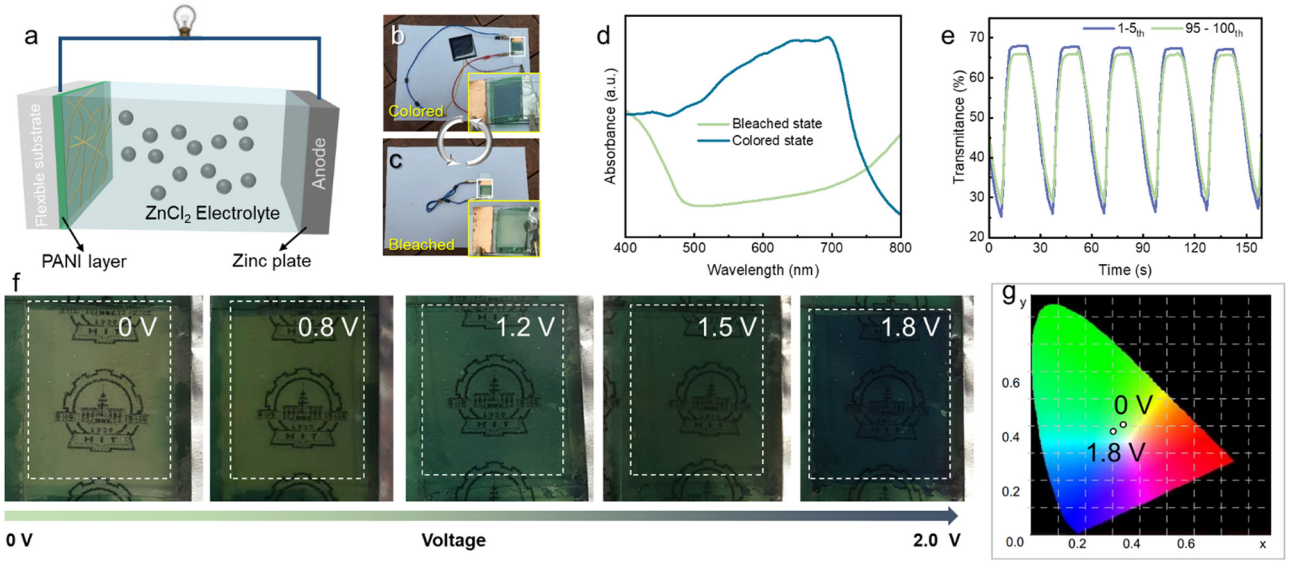


Fig. 6 (a) Schematic illustration of the configuration of the ECD based on the AgNW@Au–Co FTC using metal Zn as the counter electrode. (b) The colored state of the ECD when connected with a solar cell. (c) The bleached state of the ECD when short-circuited. (d) The UV-vis absorption spectra of the ECD in the colored and bleached states. (e) The *in situ* change in transmittance in the sweeping voltage window of 0–1.8 V. (f) The optical images of the ECD at different voltages. (g) Colorimetry of the ECD in the colored and bleached states.

Table 2 The CIE parameters of the ECD under different voltages

| Voltage | 0 V | 1.8 V |
|---|---|---|
| $L^*$ | 51.58 | 39.5 |
| $a^*$ | −12.50 | −14 |
| $b^*$ | 17.30 | 7.96 |

However, the transmittance increased to 67.37 when 0 V voltage was applied. Moreover, the ECD exhibited an optical modulation range of 41.22%. After 100 cycles of the coloring and bleaching process, the ECD still presented stable transmittance adjustment performance, as illustrated in Fig. 6e (green line). Fig. 6f demonstrates the optical images of the ECD at different voltages. With increasing voltage, the color gradually changed from light green into a deep blue, and the logo of Harbin Institute of Technology gradually became dim. We further measured the chromaticity values using the CIE system, as depicted in Table. 2. In the table, $L^*$, $a^*$ and $b^*$ are the parameters that describe the lightness, green–red and blue–yellow, respectively. The higher $L^*$ value in the bleached state indicated higher transmittance. The negative $a^*$ value suggested that the ECD showed a high degree of green at both colored and bleached states. The $b^*$ value gradually decreased from the bleached to colored state, demonstrating that the ECD had become bluer. It is obvious that the point had moved from the green region to the blue region in Fig. 6g with increasing voltage, which is also consistent with the optical images in Fig. 6f.

## Conclusions

In summary, we successfully fabricated a highly stable FTC by electrodepositing a protective Au–Co shell around the AgNW network. The resistance against chemical (remaining stable under corrosion by $H_2O_2$ for 200 s), and electrochemical corrosion (remaining stable as the electrochemical anode for 100s) was significantly improved. Moreover, because the Au and Co atoms could fill the gap between stacked NWs and weld them together, the modified electrode exhibited good optoelectrical performance (20 Ohm per sq at a high optical transparency of 87.1%) and high mechanical stability (2000 bending cycles). Besides, PANI was electropolymerized onto the AgNW@Au–Co network FTC, and a prototype flexible dual-functional electrochromic and energy-storage device was assembled using metal Zn as the counter electrode, which showed a high optical modulation range (41.22%) and good energy-storage performance (4 mF $cm^{-2}$). More importantly, the device exhibited a unique self-powering property. Our work exhibits great potential for application in next-generation multifunctional and energy-efficient flexible electronics.

## Author contributions

He Zhang: conceptualization, data curation, investigation, methodology, writing – original draft; Jiayun Feng: methodology; Fangyuan Sun: data curation, investigation; Dongyan Zhou: data curation; Ge Cao: methodology; Zhuohuan Wu: data curation, Shang Wang: conceptualization, Fengyu Su: Writing – review & editing, funding acquisition; Yanqing Tian: funding acquisition, supervision; Yanhong Tian: funding acquisition, supervision.

## Conflicts of interest

There are no conflicts of interest to declare.

## Acknowledgements

This work was supported by the National Natural Science Foundation of China (Grant No. 52175300), Heilongjiang Touyan Innovation Team Program (HITTY-20190013), Shenzhen Fundamental Research Programs (JCYJ20200925160843002) and the Start-up fund of SUSTech (Y01256114).

## References

1 H. Lee, D. Lee, Y. Ahn, E.-W. Lee, L. S. Park and Y. Lee, *Nanoscale*, 2014, **6**, 8565–8570.
2 H. Tang, H. Feng, H. Wang, X. Wan, J. Liang and Y. Chen, *ACS Appl. Mater. Interfaces*, 2019, **11**, 25330–25337.
3 N. M. Nair, I. Khanra, D. Ray and P. Swaminathan, *ACS Appl. Mater. Interfaces*, 2021, **13**, 34550–34560.
4 J. L. Sun, Y. Chang, J. Liao, S. L. Chang, S. G. Dai, Y. Y. Shang, C. X. Shan and L. Dong, *Nano Energy*, 2022, **99**, 107392.
5 J. L. Wang, S. Z. Sheng, Z. He, R. Wang, Z. Pan, H. Y. Zhao, J. W. Liu and S. H. Yu, *Nano Lett.*, 2021, **21**, 9976–9982.
6 W. J. Ye, X. Guo, X. J. Zhang and P. Liu, *Synth. Met.*, 2022, **287**, 117076.
7 W. Zhang, H. Z. Li and A. Y. Elezzabi, *Adv. Funct. Mater.*, 2022, **32**, 2108341.
8 G. Cai, R. Zhu, S. Liu, J. Wang, C. Wei, K. J. Griffith, Y. Jia and P. S. Lee, *Adv. Energy Mater.*, 2022, **12**, 2270015.
9 S. Zeb, G. Sun, Y. Nie, H. Xu, Y. Cui and X. Jiang, *Mater. Adv.*, 2021, **2**, 6839–6884.
10 H. L. Wang, S. Y. Liao, X. P. Bai, Z. L. Liu, M. H. Fang, T. Liu, N. Wang and H. Wu, *ACS Appl. Mater. Interfaces*, 2016, **8**, 32661–32666.
11 B. Bob, A. Machness, T. B. Song, H. P. Zhou, C. H. Chung and Y. Yang, *Nano Res.*, 2016, **9**, 392–400.
12 K. Qian, X. Han, H. K. Li, T. P. Chen and P. S. Lee, *ACS Appl. Mater. Interfaces*, 2020, **12**, 4579–4585.
13 Y. Qin, L. Yao, F. Zhang, R. Li, Y. Chen, Y. Chen, T. Cheng, W. Lai, B. Mi, X. Zhang and W. Huang, *ACS Appl. Mater. Interfaces*, 2022, **14**, 38021–38030.
14 S. H. Pham, A. Ferri, A. Da Costa, M. M. S. Mohan, V. D. Tran, D. C. Nguyen, P. Viville, R. Lazzaroni, R. Desfeux and P. Leclere, *Adv. Mater. Interfaces*, 2022, **9**, 2200019.
15 H. Zhang, Y. Tian, S. Wang, Y. Huang, J. Wen, C. Hang, Z. Zheng and C. Wang, *Chem. Eng. J.*, 2020, **399**, 125075.
16 W. He and C. Ye, *J. Mater. Sci. Technol.*, 2015, **31**, 581–588.
17 D. Li, T. Han, L. Zhang, H. Zhang and H. Chen, *R. Soc. Open Sci.*, 2017, **4**, 170756.
18 H. Zhang, Y. Tian, S. Wang, J. Feng, C. Hang, C. Wang, J. Ma, X. Hu, Z. Zheng and H. Dong, *Chem. Eng. J.*, 2021, **426**, 131438.
19 Y. Jin, Y. Sun, K. Wang, Y. Chen, Z. Liang, Y. Xu and F. Xiao, *Nano Res.*, 2018, **11**, 1998–2011.
20 B. Zheng, Q. Zhu and Y. Zhao, *J. Mater. Sci. Technol.*, 2021, **71**, 221–227.
21 C. Yang, Y. Tang, Z. Su, Z. Zhang and C. Fang, *J. Mater. Sci. Technol.*, 2015, **31**, 16–22.
22 A. R. Madaria, A. Kumar, F. N. Ishikawa and C. Zhou, *Nano Res.*, 2010, **3**, 564–573.
23 K. Huang, J. Liu, S. Lin, Y. Wu, E. Chen, Z. He and M. Lei, *Adv. Compos. Hybrid Mater.*, 2022, **5**, 220–228.
24 I. Chang, T. Park, J. Lee, M. H. Lee, S. H. Ko and S. W. Cha, *J. Mater. Chem. A*, 2013, **1**, 8541–8546.
25 I. Chang, T. Park, J. Lee, H. B. Lee, S. Ji, M. H. Lee, S. H. Ko and S. W. Cha, *Int. J. Hydrogen Energy*, 2014, **39**, 7422–7427.
26 T. Park, I. Chang, H. B. Lee, S. H. Ko and S. W. Cha, *Int. J. Hydrogen Energy*, 2017, **42**, 1884–1890.
27 H. Moon, H. Lee, J. Kwon, Y. D. Suh, D. K. Kim, I. Ha, J. Yeo, S. Hong and S. H. Ko, *Sci. Rep.*, 2017, **7**, 41981.
28 H. Lee, S. Hong, J. Lee, Y. D. Suh, J. Kwon, H. Moon, H. Kim, J. Yeo and S. H. Ko, *ACS Appl. Mater. Interfaces*, 2016, **8**, 15449–15458.
29 W. Hu, X. Niu, R. Zhao and Q. Pei, *Appl. Phys. Lett.*, 2013, **102**, 083303.
30 P. Won, J. J. Park, T. Lee, I. Ha, S. Han, M. Choi, J. Lee, S. Hong, K.-J. Cho and S. H. Ko, *Nano Lett.*, 2019, **19**, 6087–6096.
31 K. Park, S. Kang, J.-W. Park and J. Hwang, *J. Hazard. Mater.*, 2021, **411**, 125043.
32 S. Jeong, H. Cho, S. Han, P. Won, H. Lee, S. Hong, J. Yeo, J. Kwon and S. H. Ko, *Nano Lett.*, 2017, **17**, 4339–4346.
33 H. Kim, H. Lee, I. Ha, J. Jung, P. Won, H. Cho, J. Yeo, S. Hong, S. Han, J. Kwon, K.-J. Cho and S. H. Ko, *Adv. Funct. Mater.*, 2018, **28**, 1801847.
34 H. Kim, J. Choi, K. K. Kim, P. Won, S. Hong and S. H. Ko, *Nat. Commun.*, 2021, **12**, 4658.
35 P. Won, K. K. Kim, H. Kim, J. J. Park, I. Ha, J. Shin, J. Jung, H. Cho, J. Kwon, H. Lee and S. H. Ko, *Adv. Mater.*, 2021, **33**, 2002397.
36 H. Kim, S.-k Ahn, D. M. Mackie, J. Kwon, S. H. Kim, C. Choi, Y. H. Moon, H. B. Lee and S. H. Ko, *Mater. Today*, 2020, **41**, 243–269.
37 K. L. Zhou, C. B. Han, C. F. Li, J. Jiu, Y. Yang, L. Li, H. Wang, J. B. Liu, Z. Q. Liu, H. Yan and K. Suganuma, *ACS Appl. Mater. Interfaces*, 2018, **10**, 36128–36135.
38 J. Jung, H. Cho, R. Yuksel, D. Kim, H. Lee, J. Kwon, P. Lee, J. Yeo, S. Hong, H. E. Unalan, S. Han and S. H. Ko, *Nanoscale*, 2019, **11**, 20356–20378.
39 H. Kim, K. R. Pyun, M.-T. Lee, H. B. Lee and S. H. Ko, *Adv. Funct. Mater.*, 2022, **32**, 2110535.
40 G. Cai, P. Darmawan, M. Cui, J. Wang, J. Chen, S. Magdassi and P. S. Lee, *Adv. Energy Mater.*, 2016, **6**, 1501882.
41 I. N. Kholmanov, S. H. Domingues, H. Chou, X. Wang, C. Tan, J.-Y. Kim, H. Li, R. Piner, A. J. G. Zarbin and R. S. Ruoff, *ACS Nano*, 2013, **7**, 1811–1816.
42 M. A. Shinde and H. Kim, *Mater. Today Commun.*, 2021, **26**, 102147.
43 S. Aghazadehchors, V. H. Nguyen, D. Muñoz-Rojas, C. Jiménez, L. Rapenne, N. D. Nguyen and D. Bellet, *Nanoscale*, 2019, **11**, 19969–19979.
44 A. Khan, V. H. Nguyen, D. Muñoz-Rojas, S. Aghazadehchors, C. Jiménez, N. D. Nguyen and D. Bellet, *ACS Appl. Mater. Interfaces*, 2018, **10**, 19208–19217.

45 X. Liu, D. Li, X. Chen, W. Y. Lai and W. Huang, *ACS Appl. Mater. Interfaces*, 2018, **10**, 32536–32542.
46 H. Zhang, S. Wang, Y. Tian, Y. Liu, J. Wen, Y. Huang, C. Hang, Z. Zheng and C. Wang, *Chem. Eng. J.*, 2020, **390**, 124495.
47 P. Kumar, F. Shahzad, S. M. Hong and C. M. Koo, *RSC Adv.*, 2016, **6**, 101283–101287.
48 Q. Xu, W. Shen, Q. Huang, Y. Yang, R. Tan, K. Zhu, N. Dai and W. Song, *J. Mater. Chem. C*, 2014, **2**, 3750–3755.
49 G.-S. Liu, J.-S. Qiu, D.-H. Xu, X. Zhou, D. Zhong, H.-P. D. Shieh and B.-R. Yang, *ACS Appl. Mater. Interfaces*, 2017, **9**, 15130–15138.
50 D. Chen, J. Liang, C. Liu, G. Saldanha, F. Zhao, K. Tong, J. Liu and Q. Pei, *Adv. Funct. Mater.*, 2015, **25**, 7512–7520.
51 T.-B. Song, Y. Chen, C.-H. Chung, Y. Yang, B. Bob, H.-S. Duan, G. Li, K.-N. Tu, Y. Huang and Y. Yang, *ACS Nano*, 2014, **8**, 2804–2811.
52 T. Tokuno, M. Nogi, M. Karakawa, J. Jiu, T. T. Nge, Y. Aso and K. Suganuma, *Nano Res.*, 2011, **4**, 1215–1222.
53 T. A. Celano, D. J. Hill, X. Zhang, C. W. Pinion, J. D. Christesen, C. J. Flynn, J. R. McBride and J. F. Cahoon, *Nano Lett.*, 2016, **16**, 5241–5246.
54 J. Lee, P. Lee, H. B. Lee, S. Hong, I. Lee, J. Yeo, S. S. Lee, T.-S. Kim, D. Lee and S. H. Ko, *Adv. Funct. Mater.*, 2013, **23**, 4171–4176.
55 J. Lee, P. Lee, H. Lee, D. Lee, S. S. Lee and S. H. Ko, *Nanoscale*, 2012, **4**, 6408–6414.
56 P. Lee, J. Lee, H. Lee, J. Yeo, S. Hong, K. H. Nam, D. Lee, S. S. Lee and S. H. Ko, *Adv. Mater.*, 2012, **24**, 3326–3332.
57 S. Hong, H. Lee, J. Yeo and S. H. Ko, *Nano Today*, 2016, **11**, 547–564.
58 D. Ma, A. Lee-Sie Eh, S. Cao, P. S. Lee and J. Wang, *ACS Applied Materials & Interfaces*, 2022, **14**, 1443–1451.
59 C. Kortz, A. Hein, M. Ciobanu, L. Walder and E. Oesterschulze, *Nat. Commun.*, 2019, **10**, 4874.
60 H. Wang, C. J. Yao, H. J. Nie, L. Yang, S. L. Mei and Q. C. Zhang, *J. Mater. Chem. C*, 2020, **8**, 15507–15525.
61 Z. Q. Tong, Y. L. Tian, H. M. Zhang, X. G. Li, J. Y. Ji, H. Y. Qu, N. Li, J. P. Zhao and Y. Li, *Sci. China: Chem.*, 2017, **60**, 13–37.
62 X. Tao, Y. Zhang, J. Cai, H. H. Tan, J. Cui, Y. Wang, X. Shu, Z. Dai, Y. Qin, J. Liu and Y. Wu, *Mater. Adv.*, 2022, **3**, 7881–7893.
63 K. Zhou, H. Wang, J. Jiu, J. Liu, H. Yan and K. Suganuma, *Chem. Eng. J.*, 2018, **345**, 290–299.
64 J. Guo, X. Li, H. Liu, D. P. Young, G. Song, K. Song, J. Zhu, J. Kong and Z. Guo, *Adv. Compos. Hybrid Mater.*, 2021, **4**, 51–64.
65 H. Wei, J. Zhu, S. Wu, S. Wei and Z. Guo, *Polymer*, 2013, **54**, 1820–1831.
66 T. V. Nguyen, H. H. Do, T. Q. Trung, Q. V. Le, T. P. Nguyen, S. H. Hong, H. W. Jang, S. H. Ahn and S. Y. Kim, *J. Alloys Compd.*, 2021, **882**, 160718.
67 N. Zohrevand, T. Madrakian, A. Ghoorchian and A. Afkhami, *Electrochim. Acta*, 2022, **427**, 140856.
68 H. Wei, X. Yan, S. Wu, Z. Luo, S. Wei and Z. Guo, *J. Phys. Chem. C*, 2012, **116**, 25052–25064.
69 R. Yuksel, E. Alpugan and H. E. Unalan, *Org. Electron.*, 2018, **52**, 272–280.
70 W. Zhang, H. Li, W. W. Yu and A. Y. Elezzabi, *Small Sci.*, 2021, **1**, 2100040.
71 H. Li, W. Zhang and A. Y. Elezzabi, *Adv. Mater.*, 2020, **32**, 2003574.
72 J. Bang, S. Coskun, K. R. Pyun, D. Doganay, S. Tunca, S. Koylan, D. Kim, H. E. Unalan and S. H. Ko, *Appl. Mater. Today*, 2021, **22**, 100909.
73 I. E. Stewart, S. Ye, Z. Chen, P. F. Flowers and B. J. Wiley, *Chem. Mater.*, 2015, **27**, 7788–7794.
74 G. Luo, D. Li, G. Yuan and N. Li, *J. Electrochem. Soc.*, 2018, **165**, D107–D109.
75 M. Monev, A. Pfund, G. Beck, K. Petrov, R. Bretzler, U. Heuberger and A. Zielonka, *Trans. IMF*, 2012, **90**, 305–310.
76 T. G. Yun, M. Park, D. H. Kim, D. Kim, J. Y. Cheong, J. G. Bae, S. M. Han and I. D. Kim, *ACS Nano*, 2019, **13**, 3141–3150.
77 J.-H. Kim, H.-J. Seok, H.-J. Seo, T.-Y. Seong, J. H. Heo, S.-H. Lim, K.-J. Ahn and H.-K. Kim, *Nanoscale*, 2018, **10**, 20587–20598.
78 Y. Huang, Y. Tian, C. Hang, Y. Liu, S. Wang, M. Qi, H. Zhang and J. Zhao, *ACS Appl. Mater. Interfaces*, 2019, **11**, 21850–21858.